

Critical Role of Capping Layer in Determining Co-Fe-B/MgO Interfacial Magnetism Revealed by X-Ray Magnetic Circular Dichroism

James Lourembam^{1,2,*†} Xiaojiang Yu^{3,†} Maria Patricia Rouelli Sabino^{2,‡} Michael Tran^{2,§}
Roslyn Wan Teng Ang,⁴ Qi Jia Yap,^{1,2} Sze Ter Lim^{1,2} and Andrivo Rusydi^{3,4,5,**}


¹*Institute of Materials Research and Engineering, A*STAR (Agency for Science, Technology and Research), 2 Fusionopolis Way, Innovis, #08-03, Singapore 138634, Singapore*

²*Data Storage Institute, Agency for Science, Technology and Research (A*STAR), 2 Fusionopolis Way, #08-01 Innovis, Singapore 138634, Singapore*

³*Singapore Synchrotron Light Source, National University of Singapore, 5 Research Link, Singapore 117603, Singapore*

⁴*Department of Physics, National University of Singapore, 2 Science Drive 3, Singapore 117542, Singapore*

⁵*NUSSNI-NanoCore, National University of Singapore, Singapore 117576, Singapore*

 (Received 12 June 2020; revised 2 October 2020; accepted 5 October 2020; published 11 November 2020)

Interfacial magnetism emerging from orbital hybridization is the key facilitator for practical nanoscale spintronic devices. Most devices require a capping layer, and it is widely assumed that capping-layer variations do not change the fundamental properties of magnetic films underneath. In a model Co-Fe-B/MgO system, interfacial investigations, so far, have been focused on the hybridization of Fe *d* and O *p* orbitals. However, the role of the capping layer has largely been ignored by adopting a reductionist scenario of just oxidation or charge modification. Here, we report strong modifications of interfacial magnetism in Co-Fe-B/MgO by systematically changing the Ru capping thickness using element-specific x-ray magnetic circular dichroism and x-ray absorption spectroscopy at Fe $L_{2,3}$, Co $L_{2,3}$, and O *K* edges, along with corresponding spin and orbital magnetic moment calculations and magnetometry measurements. We observe unusual spin-flip-like transitions due to capping layers and find direct evidence for systematic spin and orbital modifications, beyond just charge transformation, strikingly captured by oxygen x-ray absorption and dichroism spectra. Our result shows the importance of the capping layer and provides a complete picture of rich interfacial magnetism in the Co-Fe-B/MgO system.

DOI: [10.1103/PhysRevApplied.14.054022](https://doi.org/10.1103/PhysRevApplied.14.054022)

I. INTRODUCTION

Rapid progress in the development of ultrathin magnetic materials for magnetic tunnel junctions (MTJs) has inspired a myriad of spintronic applications beyond magnetic random access memories (MRAMs) [1–3], including sensors [4–6], microwave generators [7], detectors [8] and amplifiers [9], voltage rectification [10], and neuromorphic computing [11,12]. For these applications, crucial MTJ features, such as strong perpendicular magnetic anisotropy (PMA) and large tunneling magnetoresistance (TMR),

have been realized on the Co-Fe-B/MgO interface [13,14]. Particularly, PMA in Co-Fe-B/MgO was attributed mainly to hybridization of the *d* orbitals of Fe atoms with the *p* orbitals of O atoms at the interface with Co atoms playing a minor role, as revealed by element-specific x-ray magnetic circular dichroism (XMCD) and first-principles calculations [13,15–18].

However, this interface is shown to be particularly susceptible to Fe oxidation and first-principles calculations show this could result in a large variation in PMA and TMR values [17,19]. Indeed, changes in the oxidation state of Fe atoms at the Co-Fe-B/MgO interface can be brought about by the annealing process [18,20–22], capping material [23], and presence or absence of boron [24]. It has always been assumed that the Co-Fe-B/MgO interface is less influenced by the capping layer in most “full-stack” MTJs, where the MgO tunneling layer is buried deep. However, the development of MTJ-free layers is typically carried out on a reduced “half-stack” structure, namely, heavy metal/Co-Fe-B/MgO/capping layer,

*james_lourembam@imre.a-star.edu.sg

†These authors contributed equally to this work.

‡Present address: Electrical and Electronics Engineering Institute, University of the Philippines Diliman, Quezon City, 1101, Philippines.

§Present address: Western Digital Research, 5601 Great Oaks Pkwy, San Jose, California 95119, USA.

**andrivo.rusydi@nus.edu.sg

while keeping the same ferromagnetic stoichiometry and annealing conditions as that of the eventual MTJ. Capping-layer parameters of the half stack are mostly dictated by the requirements of the individual experiments, which impede the development of a universal capping layer. These proceedings can also lead to nonconformities in the interpretation of the MTJ material's properties given that the capping layer strongly influences the Co-Fe-B/MgO interface. In addition, transistor-circuit current requirements and high-density applications demand high-performance MTJs with just four or fewer monolayers of MgO [25, 26]. Meanwhile, the double Co-Fe-B/MgO structure has emerged as the ideal free-layer structure for state-of-the-art MTJs for MRAM [27–29]. The introduction of a second Co-Fe-B/MgO interface, compounded by requirements for ultrathin MgO, could aggravate vulnerabilities to interfacial modifications.

A comprehensive understanding of interface modification can be achieved by tuning the effective magnetic anisotropy of half-stack structures with capping-layer parameters and establishing a direct correlation with spin and orbital coupling. By controlling the thickness of MgO/Ru, we report progressive tuning of the anisotropy from in-plane to PMA, along with element-specific changes in interfacial magnetism in the Co-Fe-B/MgO heterostructure. Ru is chosen as the capping layer due to superior a PMA performance originating from reduced intermixing and for its effectiveness against the diffusion of Ta, which is used as a popular hard mask in MTJ fabrication [23,27,30,31]. Interestingly, we find an important role of oxygen in determining spin anisotropy at the interface and unique splitting of Fe XMCD spectra, which is associated with a spin-flip-like transition in the secondary feature. In the past, the role of oxygen has been limited to dictating the oxidation state of Fe, while the possibilities of acquiring a magnetism signature through orbital charge transfer and interfacial crystal-field splitting have largely been ignored.

II. METHODS

A. Sample preparation

A series of thin films of the structure Ta(2)/Co₄₀Fe₄₀B₂₀(1)/MgO(t_{MgO})/X(t_{cap}), where $X = \text{Ta, Ru, or Pt}$, are deposited on Si substrates using the Singulus Timaris magnetron sputtering system with a vacuum base pressure of $< 5 \times 10^{-8}$ mbar. Nominal thicknesses in nanometers are shown in parentheses. The thicknesses of Ru (t_{cap}) are varied from 0 to 2 nm, while MgO thicknesses (t_{MgO}) of 1 or 3 nm are chosen. Similar t_{cap} values are used for Ta and Pt as well. All samples are annealed at 300 °C postdeposition in vacuum for 1 h. The cap materials Ta, Ru, and Pt are grown at low powers of 300, 300, and 75 W, respectively, to minimize kinetic damage to the MgO layer.

B. Magnetometry

The magnetic properties at room temperature are characterized using the alternating gradient magnetometer (AGM) after dicing into $4 \times 4 \text{ mm}^2$ area coupons using the Okamoto dicer (ADM-6D). Both in-plane (IP) and out-of-plane (OP) magnetization hysteresis loops are measured to calculate the effective magnetic anisotropy from the area enclosed by these loops [32–34]. The hysteresis loops are provided in the Supplemental Material [35].

C. X-ray absorption spectroscopy and x-ray magnetic circular dichroism

X-ray absorption spectroscopy (XAS) and XMCD are performed at room temperature and at the $L_{2,3}$ edges of Co, Fe, and O K edge in the energy ranges from 700 to 803 eV and 525 to 550 eV, respectively, at the SINS beamline of the Singapore Synchrotron Light Source [36]. A magnetic field of ± 1 T is applied parallel to the photon incident direction to attain the absorption coefficients of right and left circular polarizations, μ_+ and μ_- , respectively. The incident angles (θ), relative to the surface normal, are chosen at $\theta = 0^\circ$ and 60° to perform normal-incidence (NI) and grazing-incidence (GI) measurements, respectively. All spectra are collected in total-electron-yield (TEY) detection mode with a photon energy resolution of 0.5 eV, and the degree of the circular polarization is 88%. The probing depth is expected to be < 10 nm [20,37–41]. The XMCD signal is obtained from the difference between the absorption spectra at different helicities of circularly polarized light, μ_+ and μ_- . For μ_+ , the majority of electron spin is parallel to circular helicity, whereas for μ_- the majority of electron spin is antiparallel to circular helicity. The spectra are normalized against the incoming photon beam intensity (I_0), which measures the photocurrent of the last gold-coated mirror on the beamline. The correction of saturation effects following Nakajima *et al.* [42] is discussed in the Supplemental Material [35].

III. RESULTS AND DISCUSSIONS

A. Modulation of anisotropy energy with $\Delta t_{\text{interface}}$

Figure 1(a) shows a comparison of the effective magnetic anisotropy, K_{eff} , for various capping materials, X , in the sample set Ta(2)/Co-Fe-B(1)/MgO(1)/X(1), where $X = \text{Ta, Ru, or Pt}$. In subsequent discussions, Co₄₀Fe₄₀B₂₀ composition is represented by Co-Fe-B unless otherwise mentioned. We see that Ru capping displays the strongest PMA, in agreement with a previous report [23]. In this study, we choose to focus on the role of capping thickness, since there is a general trend of stronger PMA with thicker capping. This is true even for Pt, which becomes PMA when the thickness becomes > 1.2 nm. The thickness-dependent K_{eff} data are shown in the Supplemental Material [35]. The rest of the discussion is based on the

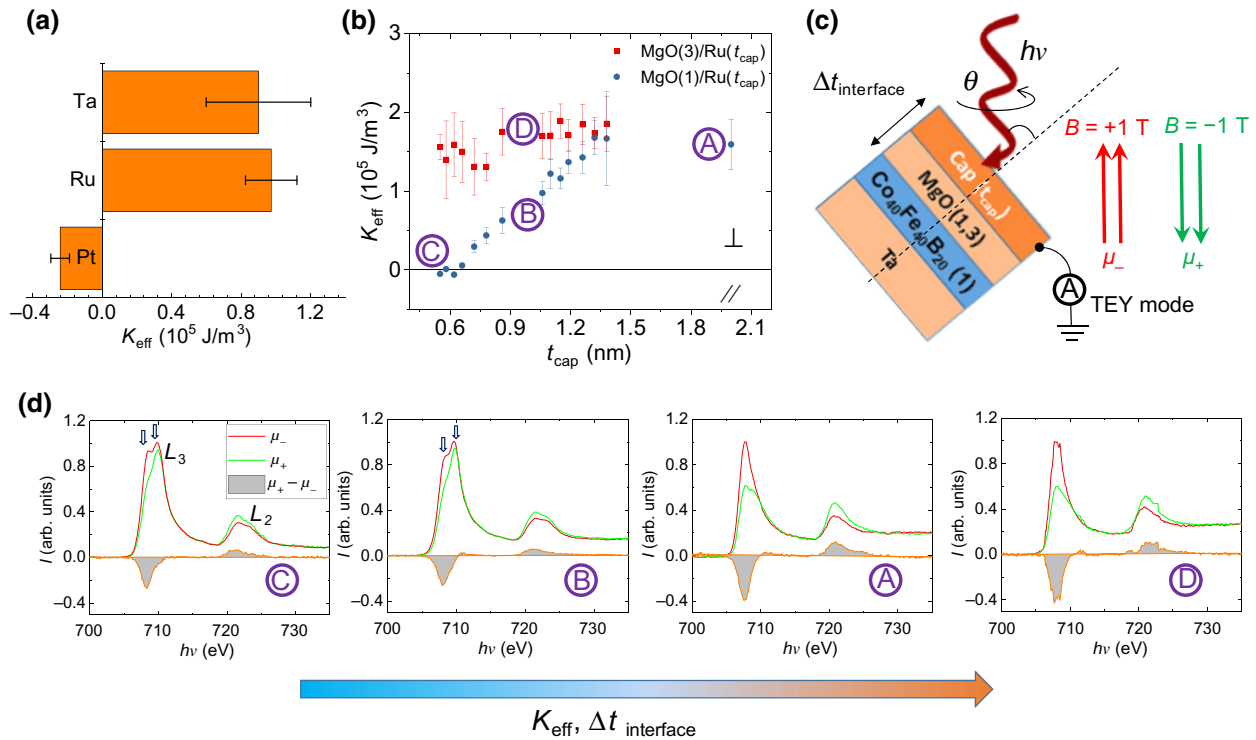


FIG. 1. Modulation of anisotropy energy with $\Delta t_{\text{interface}}$. (a) Comparison of effective magnetic anisotropies of various samples of Ta(2)/Co-Fe-B(1)/MgO(1)/ X (1), where $X = \text{Ta, Ru, or Pt}$. (b) Effective magnetic anisotropy, as measured using an AGM for various Ru capping-layer thicknesses. Samples **A**, **B**, **C**, and **D** represent those selected for XAS and XMCD measurements. (c) Schematic representation of XAS and XMCD measurements on Co-Fe-B/MgO samples with various caps. μ_+ and μ_- represent absorption coefficients for different helicities. (d) From left to right, XAS and corresponding XMCD Fe spectra taken at $\theta = 0^\circ$ for samples with increasing K_{eff} and increasing $\Delta t_{\text{interface}}$. Two down arrows in samples **C** and **B** indicate splitting of the L_3 edge in the Fe spectra.

Ru capping layer, unless otherwise mentioned. To understand the role of the capping layer, we first design and determine K_{eff} with varying Ru thicknesses (t_{cap}). For the set of samples with Ta(2)/Co-Fe-B(1)/MgO(1)/Ru(t_{cap}), we observe that K_{eff} goes from IP to PMA and systematically becomes more positive with thicker t_{cap} for $0.4 \text{ nm} < t_{\text{cap}} < 1.35 \text{ nm}$ [Fig. 1(b)]. The system eventually reaches a maximum PMA of about $1.8 \times 10^5 \text{ J/m}^3$. On the other hand, for the 3-nm-thick MgO sample set, Ta(2)/Co-Fe-B(1)/MgO(3)/Ru(t_{cap}), no dependence on t_{cap} for $0.4 \text{ nm} < t_{\text{cap}} < 1.35 \text{ nm}$ is found. Dependence on both MgO and Ru thicknesses suggests that both t_{cap} and the effective depth of the Co-Fe-B/MgO interface ($\Delta t_{\text{interface}} = t_{\text{MgO}} + t_{\text{cap}}$) play important roles in engineering a categorical interface specifically at ultrathin thicknesses.

The experimental geometry for XMCD is shown in Fig. 1(c) to describe the incidence angle and photon helicity direction. The photon incidence direction is parallel to the applied magnetic field. We investigate the origin of this modulation at the Co-Fe-B/MgO interface from XAS and XMCD experiments by selecting samples with increasing K_{eff} , which are measured at $\theta = 0^\circ$ incidence [Fig. 1(d)].

A common feature of the XAS spectra reveals the Fe $2p \rightarrow 3d$ x-ray dipole-allowed transition, which peaks for the L_2 edge ($2p_{3/2} \rightarrow 3d$) at about 721.1 eV and the L_3 edge ($2p_{1/2} \rightarrow 3d$) at about 708.3 eV [40]. As a result, one can clearly see that the strength of the XMCD signal increases for samples with increasing K_{eff} . Interestingly, for samples with small $\Delta t_{\text{interface}}$ or weak K_{eff} , a peak splitting is observed in the Fe L_3 XAS edge. Notably, this feature cannot be explained by the existence of Fe oxides, such as $\gamma\text{-Fe}_2\text{O}_3$; instead, our system shows three significant differences, namely, (i) the components of the L_3 spectra are equal in strength, (ii) no splits in Fe L_2 are observable, and (iii) XMCD does not show a significant peak splitting at the corresponding energies [18,40,43,44]. Furthermore, we do not see peak splitting in the Co XAS spectra (provided in the Supplemental Material [35]), which is expected, since the enthalpy of Fe—O bond formation is energetically favorable over that of Co—O bond formation [20]. All of these differences further emphasize that our observed peak splitting is unique to the interface and is different from bulk Fe oxide spectra. Moreover, previous XMCD measurements show that the interfacial magnetic

anisotropy in these systems is mainly brought by the Fe $3d$ orbital moments, and so, subsequent sections focus on the analysis of Fe spectra [15].

B. X-ray absorption and x-ray magnetic circular dichroism at Fe $L_{2,3}$ edges revealing interfacial anisotropy

The peak splitting of Fe spectra observed in both NI and GI configurations for samples ③ and ④ are shown in Figs. 2(a), 2(d) and 2(b), 2(e), respectively. Also, as with $\theta = 0^\circ$ incidence, the XMCD strength taken in $\theta = 60^\circ$ incidence increases for samples with larger K_{eff} . However, the XMCD signal for sample ③ in the GI configuration has an extra positive feature [Fig. 2(d)] near the Fe L_3 absorption edge that is reminiscent of antiparallel spin orientation sites in $\gamma\text{-Fe}_2\text{O}_3$ or the presence of tetrahedral (T_d) Fe^{3+} in nanostructured Fe_3O_4 [44,45].

The anisotropy of the orbital magnetic moments can be revealed from the asymmetry in different measurement configurations (NI and GI). The dashed lines in Fig. 2

show normalized integrated XMCD spectra. The integral parameters p and q indicated in Fig. 2(a) correspond to the integrated values of L_3 and $L_2 + L_3$ spectra respectively, which are used in the sum-rule analysis of spin and orbital moments given by [46,47]

$$\mu_{\text{eff}} = \mu_S + 7 \mu_T$$

$$= -\frac{2n_h\mu_B \left[\int_{L_3} (\mu_+ - \mu_-) d\omega - 2 \int_{L_2} (\mu_+ - \mu_-) d\omega \right]}{\int_{L_{2,3}} (\mu_+ + \mu_-) d\omega}$$

$$\mu_L = -\frac{4n_h\mu_B \int_{L_{2,3}} (\mu_+ - \mu_-) d\omega}{3 \int_{L_{2,3}} (\mu_+ + \mu_-) d\omega},$$

where μ_{eff} , μ_S , μ_T , and μ_L are the effective spin magnetic moment, spin magnetic moment, intra-atomic magnetic dipole moment, and orbital magnetic moment, respectively. Notably, μ_T is negligibly small and not considered in the calculations. μ_B is the Bohr magneton and n_h represents the $3d$ holes per atom, which is taken to be 3.39

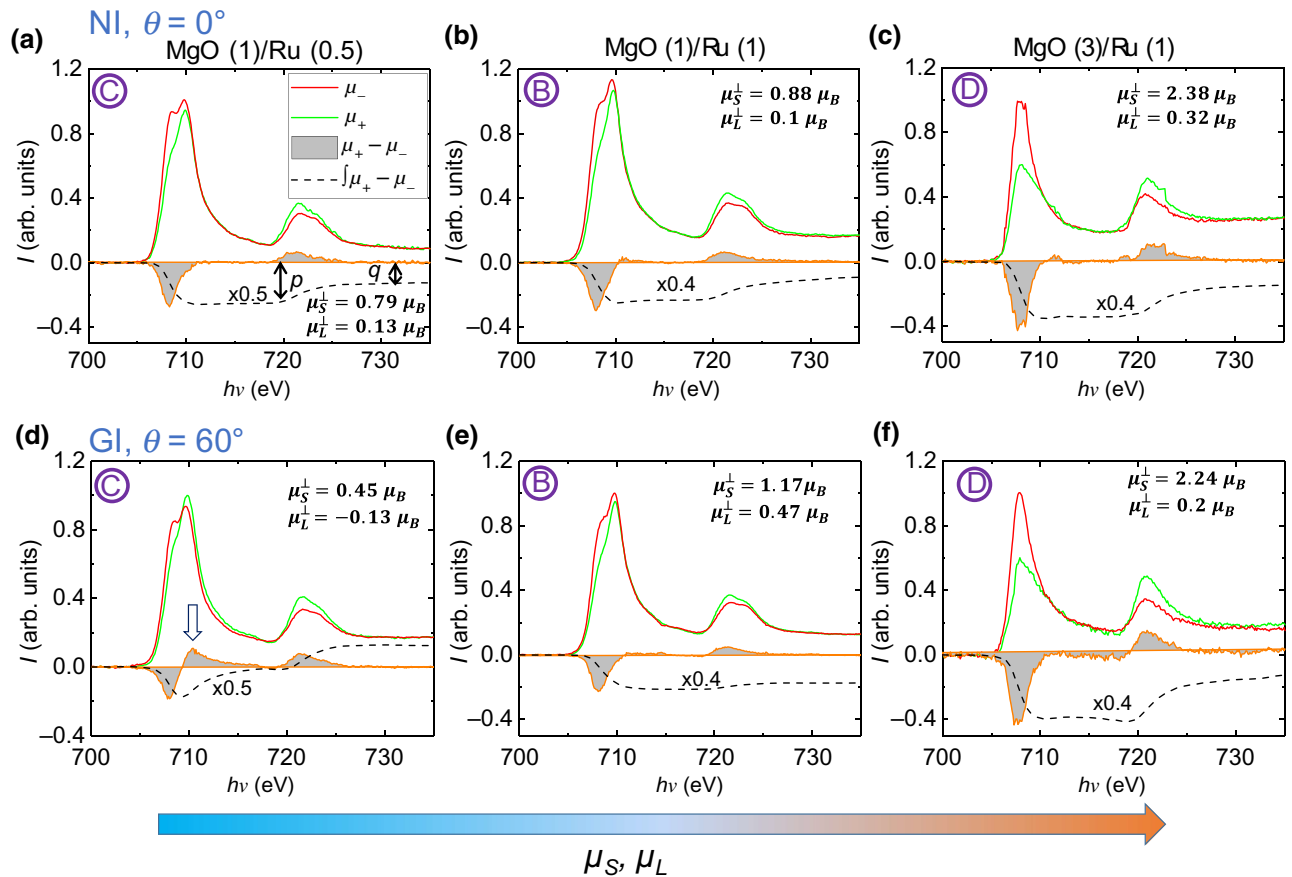


FIG. 2. Fe $L_{2,3}$ edges across improving interfacial anisotropy. XAS and XMCD spectra taken at normal incidence ($\theta = 0^\circ$) for samples ③, ④, and ⑤ at Fe $L_{2,3}$ edge are shown in (a)–(c), respectively. For grazing angle ($\theta = 60^\circ$), corresponding spectra for ③, ④, and ⑤ are shown in (d)–(f), respectively. Corresponding numerical integral of XMCD spectra is traced by the dashed black lines. Also shown are the spin and orbital moments for each of the samples at incidences $\theta = 0^\circ$ and 60° , which are calculated using conventional sum-rule analysis from integral parameters p and q , as shown in (a) as an illustration.

for Fe and 2.49 for Co [47]. We first discuss a scenario where there are only Fe and Co atoms and no ionic species are considered. The evaluated spin and orbital moments for Fe for various samples in units of μ_B/atom are shown in Fig. 2, with superscript \perp and \parallel denoting values at NI and GI, respectively. We observe that the positive strengths in both μ_S and μ_L increase as one moves through samples \textcircled{C} , \textcircled{B} , and \textcircled{D} accordingly. This order is the same as that of increasing K_{eff} or $\Delta t_{\text{interface}}$ and follows in both $\theta = 0^\circ$ and 60° incidence. For bulk Fe, μ_S and μ_L are about $2 \mu_B$ and about $0.09 \mu_B$, respectively [47]. Interestingly, μ_L in all our samples is higher than this bulk value, even for the weakest K_{eff} , but μ_S is higher only for sample \textcircled{D} . This shows that interfacial orbital contributions occur for all samples. Sample \textcircled{D} , which has the largest $\Delta t_{\text{interface}}$, also shows the highest μ_L^\perp/μ_S^\perp ratio (~ 0.16). The spin and orbital moments in sample \textcircled{D} are larger than those of previous XMCD-determined values in Co-Fe-B(0.85, 2)/MgO(1)/Ta(1), which are $\mu_S^\perp \sim 1.6 \mu_B$ and $\mu_L^\perp \sim 0.3 \mu_B$ [15], and are due to the effect of the capping layer. This result is different from that of Fe/MgO film heterostructures, which have comparable μ_S , but a much weaker μ_L , similar to bulk Fe values [48,49]. At the same time, “isolated” Fe atoms on MgO display much stronger PMA and larger μ_L , by 10 times, in comparison to Fe/MgO films and seem to be closer to our results [50]. This strong PMA has been argued to be a result of the interplay between the low-symmetry ligand field and spin-orbit coupling. Our results show that the presence of this interplay at the Co-Fe-B/MgO interface is uniquely different from Fe/MgO heterostructures with weak μ_L .

Therefore, $\Delta t_{\text{interface}} \geq 4$ nm introduces a strong hybridization of Fe d orbitals at the interface and this hybridization still exists even at $\Delta t_{\text{interface}} = 1.5$ nm. At the same time, for samples \textcircled{C} and \textcircled{B} , because of the large difference of μ_S with bulk values, one clearly needs to revisit moment calculations by considering two Fe components. A thorough discussion of the magnetic moments, by adopting two-component analysis, is provided in Sec. III D.

C. Anisotropy modulation revealed by charge transfer of d orbitals

Our key results on interfacial charge transfer of d electrons and hybridization strength with varying $\Delta t_{\text{interface}}$ can be understood from the O K -edge XAS and XMCD measurements. Figures 3(a)–3(d) show XAS spectra (top panel) of O K edge and XMCD (bottom panel) at $\theta = 0^\circ$ and 60° incidences for various $\Delta t_{\text{interface}}$ samples. The O spectral region between 528 and 533 eV is typically described by the hybridization of O $2p$ and transition-metal (TM) $3d$ bands [51]. The appearance of two similar peaks in this preedge region is attributed to the splitting of minority TM $3d$ bands into low-lying t_{2g} and high-lying e_g orbitals from the octahedral crystal field [52].

In our case, we do not observe significant double peaks for samples \textcircled{E} , which is Ta(2)/Co-Fe-B(1)/MgO(3), and \textcircled{C} [Figs. 3(a) and 3(b)]. Meanwhile, double peaks appear for samples \textcircled{B} and \textcircled{D} , as shown by the down arrows in Figs. 3(c) and 3(d), respectively, likely due to the crystal-field splitting and stronger hybridization of Fe $3d$ and O p orbitals [40]. Notably, strong hybridization significantly modifies the electronic bands, giving rise to an interfacial crystal field [17,53]. The peak separation in the preedge region is about 2.3 eV, which is much larger than that of bulk Fe oxides such as Fe_2O_3 (~ 1.3 eV) and GaFeO_3 (~ 1.4 eV), and indicates the presence of a strong interfacial crystal field [40,51]. In an octahedral crystal-field-splitting scenario, lower energy t_{2g} comprises of d_{xy} , d_{yz} , and d_{xz} orbitals, whereas higher energy e_g consists of d_{z^2} and $d_{x^2-y^2}$ orbitals. First-principles calculations indicate that the origin of PMA at the Fe/MgO interface is hybridization between Fe d_{z^2} and O p_z orbitals combined with hybridization between Fe d_{xy} , d_{yz} , and d_{z^2} orbitals [17]. For samples \textcircled{B} and \textcircled{D} , the t_{2g} component increases at $\theta = 60^\circ$ incidence. The O preedge spectra comparison at $\theta = 0^\circ$ and 60° incidence is shown in the Supplemental Material [35]. Similarly for sample \textcircled{C} , lifting of d -orbital degeneracy is visible at $\theta = 60^\circ$ incidence, even though the feature is not observable at $\theta = 0^\circ$ incidence. Our GI measurements suggest additional orbital hybridization along the film plane.

Crucially, deeper insights into interfacial magnetism are revealed by the XMCD spectra at the O K edge, which is largely ignored in Co-Fe-B/MgO heterostructures. For sample \textcircled{D} , the interface of which is most protected as $\Delta t_{\text{interface}}$ is largest, one can see a significant negative XMCD peak at about 530 eV and a positive peak at about 534 eV for $\theta = 60^\circ$ incidence [Fig. 3(d)]. The negative peak at about 530 eV is typically associated with a double exchange of octahedral Fe orbitals of different species via O $2p$ orbital bonding [45,54]. The dichroism in O comes from electrons in Fe species hopping from one site to another, as shown in Fig. 3(f). In this case, hopping is between Fe species of the same spin-moment direction. On the other hand, the positive peak at about 534 eV might correspond to the asymmetrical superexchange interaction of different Fe species with different spin-moment directions via O orbitals [45,54]. However, the positive peak in our samples is at slightly higher energy than that of Fe_3O_4 films, which is at about 532 eV. At $\theta = 0^\circ$ incidence, the features are significantly diminished. In sample \textcircled{C} , we see a weaker negative peak at about 530 eV for both incidences, indicating that charge transfer from Fe d to O p orbitals is still present [Fig. 3(c)]. Interestingly, for low- K_{eff} samples [Figs. 3(a) and 3(b)], we see that the negative peak moves to higher energies of 538–545 eV. This reveals that hybridizations between Co d and O p orbitals are enhanced and yield charge transfer from Co, as illustrated in Fig. 3(e). Evidently, the Co orbital moment in

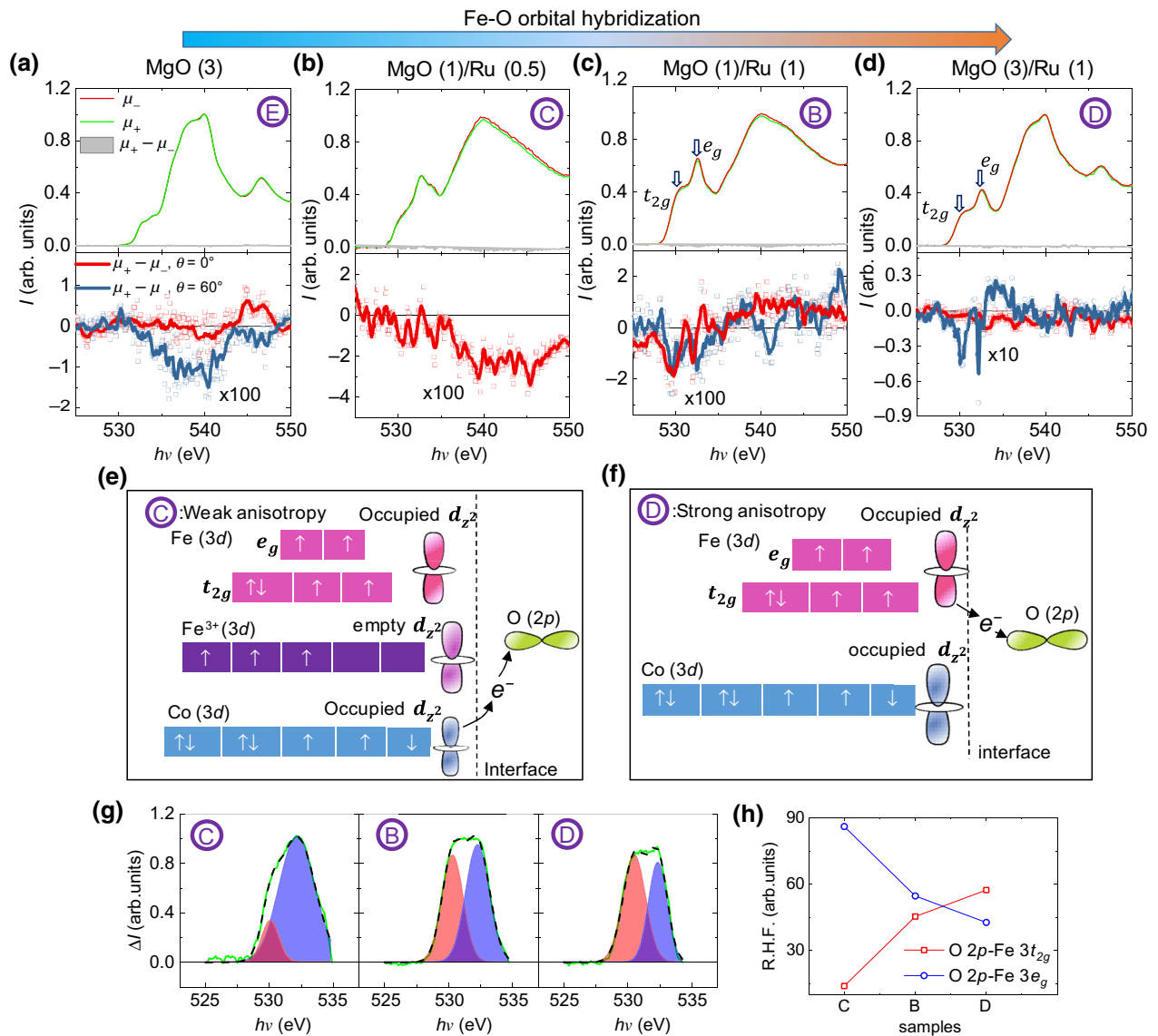


FIG. 3. Anisotropy modulation as revealed by charge transfer of d orbitals. Top panels of (a)–(d) show XAS and XMCD spectra at O K edge, at $\theta = 0^\circ$ incidence for samples with capping layers MgO(3), MgO(1)/Ru(0.5), MgO(1)/Ru(1), and MgO(3)/Ru(1), respectively. Down arrows in (c) and (d) indicate e_g and t_{2g} levels. Bottom panel shows corresponding magnified XMCD at $\theta = 0^\circ$ (red) and 60° (blue) incidence. XMCD line plots are derived by local averaging of XMCD data points (symbols) to smooth data. (e) Schematic illustration depicting the choice of charge transfer from Co d to O p orbitals in sample ©. (f) Illustration of charge transfer from Fe d orbital to O p orbital in sample ④, which results in strong anisotropy. Also shown are d orbitals of other relevant species present in the sample. (g) XAS intensities, green lines, in the O preedge region in μ_+ helicities after subtracting reference spectra as background for samples ©, ③, and ④. Dashed lines indicate total fitting using two Gaussians. (h) Relative hybridization factors for O p -Fe t_{2g} and O p -Fe e_g , as obtained from integrated intensities of fittings in (g) shown by red and blue shaded areas, respectively.

sample © displays strong anisotropy and is quite large, showing a value of $0.23 \mu_B$, as opposed to $0.16 \mu_B$ in sample ④. Co moment calculations are provided in the Supplemental Material [35]. Notably, peaks for Co $L_{2,3}$ edges are seen at higher energies of about 794 and 780 eV, respectively, when compared with that of Fe.

The strength of hybridizations of O $2p$ and TM $3d$ orbitals at the interface can be assessed by the integrated

intensities of the O K preedge region after subtraction of the linear background [55,56]. The change in the relative strength of hybridization with t_{cap} is investigated by taking sample © as the reference sample. The reference sample shares common deposition conditions, while its preedge spectral features, although not perfectly identical, share similarities with the spectrum of characteristic MgO [21,57]. The subtracted intensities for samples ©, ③, and

Ⓓ are shown in Fig. 3(h), along with two Gaussian fittings. The t_{2g} and e_g relative hybridization factors (R.H.F.s) are then determined from the integrated Gaussian components. R.H.F. is plotted normalized to the total area under the curve. Notably, we are not able to compare the R.H.F.s of t_{2g} or e_g across samples due to different x-ray attenuation for different Ru capping thicknesses, but we can compare these bands within the same sample. Remarkably, we find that, as K_{eff} becomes stronger, the R.H.F. of t_{2g} becomes stronger than that of e_g .

D. Component analysis of Fe L_3 edge

Next, we perform quantitative analysis of spin and orbital magnetic moments in samples where $\Delta t_{\text{interface}} < 3$ nm, i.e., Ⓒ and Ⓓ, which show peak splitting in the Fe L_3 edge. Spectral component analysis is shown for sample Ⓓ in Figs. 4(a) and 4(b) taken at $\theta = 0^\circ$ incidence at μ_- and μ_+ polarizations, respectively. The components are

labeled Fe^A and Fe^I , corresponding to lower and higher energies, respectively. A reference sample with no doublet feature in Fe, in this case, sample Ⓔ, is taken and the Fe $L_{2,3}$ spectrum is fitted to determine component Fe^A . The spectra for sample Ⓔ are provided in the Supplemental Material [35]. Next, the Fe^A component is scaled down to get the best fit for the particular sample being analyzed. Finally, component Fe^I is determined by subtracting the best-fit component A from the spectra. This analysis restricts component Fe^A to metallic Fe atoms, while feature Fe^I can be attributed to interfacial Fe—O bonds. Essentially, component Fe^I acts like a thin layer interface between component Fe^A and the MgO layer. This classification agrees well with the fact that a stronger Fe^I spectrum is expected (i) for sample Ⓒ, which is more susceptible to oxidation, and (ii) at $\theta = 60^\circ$ incidence due to a finite escape depth of the photoelectrons.

The spin moments of component Fe^A determined from the sum-rule analysis are 1.86 and 2.1 μ_B for $\theta = 0^\circ$

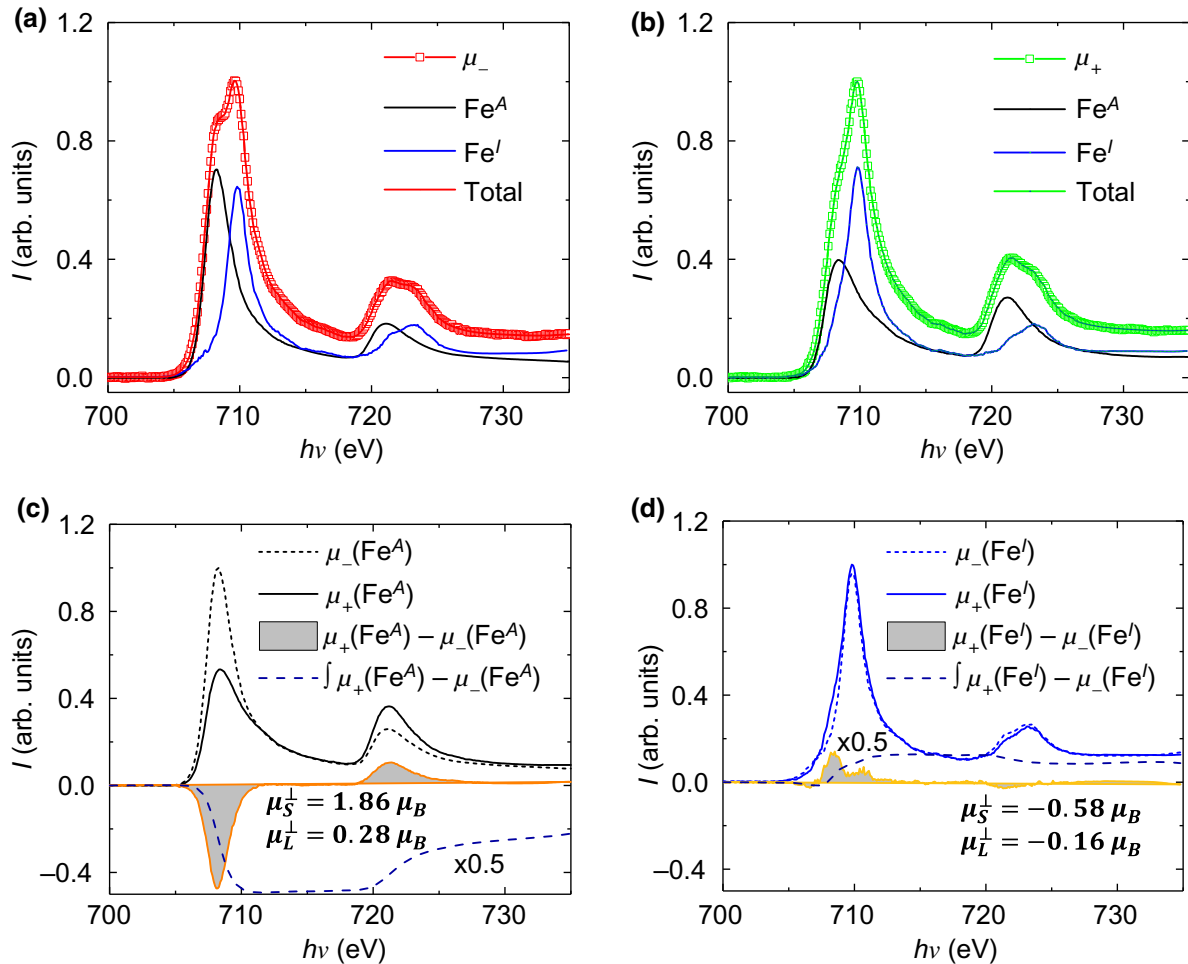


FIG. 4. Component analysis of Fe L_3 edge. XAS spectra for sample Ⓓ at Fe $L_{2,3}$ edge for polarization μ_- and μ_+ are shown in (a),(b), respectively, taken at NI. Black and blue curves represent components Fe^A and Fe^I , which are used to give the total fit. (c) XAS, XMCD, and integral XMCD of component Fe^A , along with spin and moment calculations. (d) Similar moment calculations are also performed for component Fe^I .

[Fig. 4(c)] and 60° incidence, respectively, which are close to those of metal Fe atoms. Intriguingly, the XMCD intensities at $L_{2,3}$ edges of component Fe^I are reversed to that of Fe^A [Figs. 4(c) and 4(d)]. This reveals that the majority of electron spins of components Fe^A and Fe^I are aligned in opposite directions, suggesting a spin-flip-like transition in component Fe^I . Spin-flipping phenomena may occur in Fe oxides when ionic Fe occupies T_d sites, which opposes spins in the octahedral sites (O_h) [45]. The presence of a small ionic Fe species at T_d sites is also supported by the positive XMCD peak in sample © [Fig. 2(d)] [45]. This spin-flipping phenomenon lowers the magnetic anisotropy and explains the smaller K_{eff} found in smaller t_{cap} samples. In contrast, for sample ④, where $\Delta t_{\text{interface}} = 4$ nm, neither Fe $L_{2,3}$ peak splitting nor a spin-flip-like transition is evident; hence, occupancy at T_d sites is unlikely in this sample [58].

The exact valence state of Fe in component Fe^I is inherently complex in character, due to it being an interfacial phenomenon. Also, the ionic Fe species at the interface are likely to have empty d_{z^2} orbitals, the primary orbital involved in PMA for this system, and hence, will not participate in charge transfer to $O p$ orbitals [Fig. 3(e)]. On the same sample ④, Co $L_{2,3}$ edges do not show peak-splitting features and the calculated spin moments, using a single component, gives $0.57 \mu_B$ ($\theta = 0^\circ$) and $0.91 \mu_B$ ($\theta = 60^\circ$), which agree with expected values [15].

E. Anisotropy of spin and orbital magnetic moments

The comprehensive set of spin and orbital moments from individual and combined components Fe^A and Fe^I in Fe spectra for various samples at both NI and GI incidences are summarized in Table I. For component Fe^A , we take n_h to be that of Fe and, for component B , we assume it to be similar to $\gamma\text{-Fe}_2\text{O}_3$ and is calculated to be 12.5333 [40]. The exact value of n_h in component Fe^I is difficult to determine. As expected for sample ©, which shows in-plane magnetic anisotropy characteristics, μ_S^{\parallel} and μ_L^{\parallel} values from the Fe^I component are larger than those of μ_S^{\perp} and μ_L^{\perp} , respectively. Also, both magnetic moments for the Fe^I component become more negative as the magnetic anisotropy becomes more in-plane. It is noteworthy to mention that first-principles calculations predict that the presence of interfacial Fe oxide will reduce the overall PMA in Co-Fe/MgO or Fe/MgO systems [17,59].

One can clearly identify anisotropy (moment difference between NI and GI incidence) trends across these samples by looking at the total $\text{Fe}^A + \text{Fe}^I$ values. XMCD anisotropy in both total μ_S and μ_L follows the order ④ $>$ ③, which is the same order as that of K_{eff} or $\Delta t_{\text{interface}}$. In sample ©, total μ_S^{\parallel} remains small, at $0.41 \mu_B$, and the negative sign in μ_L^{\parallel} persists, as seen for single-component analysis, which complicates the comparison. However, we see that, by adopting component analysis, the unusually low

TABLE I. Comparison of Fe component analysis across various samples.

Sample	$\theta = 0^\circ$ (μ_B)						$\theta = 60^\circ$ (μ_B)					
	Fe^A		Fe^I		$\text{Fe}^A + \text{Fe}^I$		Fe^A		Fe^I		$\text{Fe}^A + \text{Fe}^I$	
	μ_S^{\perp}	$\mu_L^{\perp}/\mu_S^{\perp}$	μ_S^{\perp}	$\mu_L^{\perp}/\mu_S^{\perp}$	μ_S^{\perp}	$\mu_L^{\perp}/\mu_S^{\perp}$	μ_S^{\parallel}	$\mu_L^{\parallel}/\mu_S^{\parallel}$	μ_S^{\parallel}	$\mu_L^{\parallel}/\mu_S^{\parallel}$	μ_S^{\parallel}	$\mu_L^{\parallel}/\mu_S^{\parallel}$
④	0.32	2.38	0.13	0.32	2.38	0.13	0.2	2.24	0.09	0.2	2.24	0.09
③	0.28	1.86	0.15	0.12	1.28	0.09	0.47	2.1	0.22	-0.11	-0.69	0.16
©	0.5	1.93	0.26	0.28	1.58	0.18	0.13	1.68	0.07	-0.47	-1.27	0.37

values of μ_S , as determined in Fig. 2, are corrected to reasonable values of $>1.6 \mu_B$ for component Fe^4 . These moment values are also more realistic than those obtained from calculations where only $\gamma\text{-Fe}_2\text{O}_3$ is considered (see Supplemental Material [35]).

F. Disentangling effects of MgO and Ru

Finally, we seek to disentangle the effects of MgO and Ru layers on the Co-Fe-B/MgO interface by adding the XAS and XMCD spectra from the film stack Ta(2)/Co-Fe-B(1)/MgO(1), labeled as sample \textcircled{F} . This gives us a set of samples capped with MgO(1), MgO(1)/Ru(0.5) [sample \textcircled{C}], and MgO(1)/Ru(1) [sample \textcircled{B}], allowing us to isolate the role of the Ru capping layer at a constant MgO thickness. Figure 5(a) shows the XAS O 1s spectra comparing samples \textcircled{F} , \textcircled{C} , and \textcircled{B} . A characteristic peak at about 546.5 eV for bulklike MgO, also found in our MgO(3) and MgO(3)/Ru(1) capping films, is missing in the MgO(1)-capped set of films [21,57]. Interestingly, the preedge region (527–535 eV) is noticeably different in sample \textcircled{F} from the rest. As discussed in previous sections, this preedge region gives us

crucial evidence for interfacial Fe and O orbital hybridization, octahedral crystal-field splitting, and charge transfer of d electrons. We perform further analysis in this preedge region by subtracting the background (as discussed in the Supplemental Material [35]), followed by normalization with the corresponding integrated intensity [60]. These normalized spectra are plotted in Fig. 5(b), where three distinct features are observed P_1 (~ 530.5 eV), P_2 (~ 532.6 eV), and P_3 (~ 534 eV). P_1 and P_2 correspond to hybridized low-lying t_{2g} and high-lying e_g orbitals respectively, while P_3 might be of MgO origin. Two remarkable observations are found from Fig. 5(b). First, the P_1 feature is nonexistent in the MgO(1) sample. Second, when the thickness of Ru increases from 0 to 1 nm, the intensities of features P_1 and P_2 increase dramatically. These observations provide strong evidence that Ru capping is crucial to realize enhanced hybridization of Fe $3d$ and O $2p$ orbitals.

We further investigate the Fe and Co XAS and XMCD spectra in sample \textcircled{F} to fully understand the effects of MgO and Ru capping layers. Figures 5(c) and 5(d) show XAS and XMCD data at Fe $L_{2,3}$ and Co $L_{2,3}$ edges, respectively, taken at NI incidence. The Fe L_3 doublet

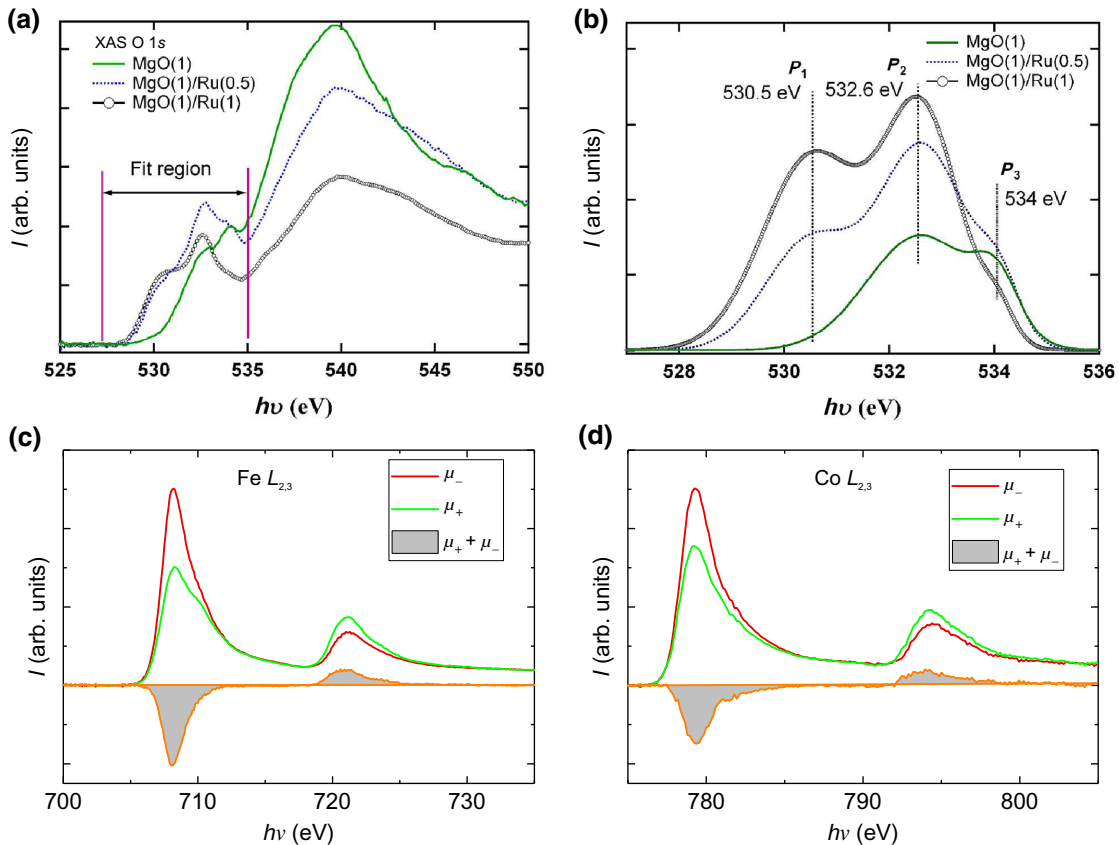


FIG. 5. Spectral disentangling of MgO and Ru effects. (a) XAS spectra at O K edge, at $\theta = 0^\circ$ incidence, for samples with capping layers MgO(1) [sample \textcircled{F}], MgO(1)/Ru(0.5), and MgO(1)/Ru(1). (b) Comparison of normalized preedge O spectra (527–535 eV) of the same set of samples after background subtraction. XAS and XMCD spectra for MgO(1)-capped film at (c) Fe $L_{2,3}$ and (d) Co $L_{2,3}$ edges.

features are vanishingly small in MgO(1) capping. We recount that Fe L_3 doublet features are strongly visible in MgO(1)/Ru(0.5) [sample ©] and MgO(1)/Ru(1) [sample ②] capping films, and the intensity of the Fe L component is most profound in sample ② [Figs. 2(a) and 2(b)]. These observations are strongly correlated with the comparison of hybridization strengths in shown in Fig. 5(b). Crucially, we infer that the spin-flip-like transition seen in samples ② and © with Ru capping is not observable in one without Ru capping. On the other hand, the Co XAS and XMCD spectra of MgO(1) show no qualitative differences from those of MgO(1)/Ru(0.5) and MgO(1)/Ru(1) capping films.

IV. SUMMARY

We show the crucial role of the Ru capping layer, disentangling MgO layer effects, in determining the magnetic properties of Co-Fe-B/MgO interface from strong PMA to weakly in-plane, originating from the interplay between charge, spin, and orbital modification of primarily Fe species in this system. With thorough element-specific experiments supported by corresponding model calculations, we establish a critical depth thickness of 4 nm from the Co-Fe-B/MgO interface as a universal baseline for reliable half-stack studies and the importance of oxygen in the magnetic anisotropy and spin-flipping-like phenomenon at the interface. Our findings, which go beyond interfacial orbital hybridization to include the interfacial crystal field, component analysis of XMCD, spin-flip-like transitions, and charge transfer of d electrons, provide pathways to tune the properties of MTJs through oxygen and interface engineering.

ACKNOWLEDGMENTS

This work is supported by the Ministry of Education of Singapore (MOE) AcRF Tier-2 (Grants No. MOE2017-T2-1-135, No. MOE2018-T2-2-117, and No. MOE2019-T2-1-163), MOE AcRF Tier-1 (Grants No. R-144-000-423-114 and No. R-144-000-398-114), and NUS Core Support (Grant No. C-380-003-003-001). The work at A*STAR is funded by the core fund (CF-16) and SpOT-LITE program (A*STAR Grant No. A18A6b0057) through RIE2020 funds from Singapore. The authors also thank the Singapore Synchrotron Light Source (SSLS) for providing the facility necessary for conducting the research. SSLS is a National Research Infrastructure under the Singapore National Research Foundation. We thank Hang Khume Tan for help in film deposition.

[1] L. Thomas, G. Jan, J. Zhu, H. Liu, Y. J. Lee, S. Le, R. Y. Tong, K. Pi, Y. J. Wang, D. Shen, R. He, J. Haq, J. Teng, V. Lam, K. Huang, T. Zhong, T. Torng, and P. K. Wang,

Perpendicular spin transfer torque magnetic random access memories with high spin torque efficiency and thermal stability for embedded applications (invited), *J. Appl. Phys.* **115**, 172615 (2014).

- [2] D. Apalkov, B. Dieny, and J. M. Slaughter, Magnetoresistive random access memory, *Proc. IEEE* **104**, 1796 (2016).
- [3] S. Yuasa *et al.*, in *2013 IEEE International Electron Devices Meeting* (Washington, DC, 2013), pp. 3.1.1.
- [4] Y. Fuji, S. Kaji, M. Hara, Y. Higashi, A. Hori, K. Okamoto, T. Nagata, S. Baba, A. Yuzawa, K. Otsu, K. Masunishi, T. Ono, and H. Fukuzawa, Highly sensitive spintronic strain-gauge sensor based on a MgO magnetic tunnel junction with an amorphous CoFeB sensing layer, *Appl. Phys. Lett.* **112**, 062405 (2018).
- [5] T. Takenaga, Y. Tsuzaki, C. Yoshida, Y. Yamazaki, A. Hatada, M. Nakabayashi, Y. Iba, A. Takahashi, H. Noshiro, K. Tsunoda, M. Aoki, T. Furukawa, H. Fukumoto, and T. Sugi, Magnetic tunnel junctions for magnetic field sensor by using CoFeB sensing layer capped with MgO film, *J. Appl. Phys.* **115**, 17E524 (2014).
- [6] H. F. Yang, X. K. Hu, N. Liebing, T. Böhnert, J. D. Costa, M. Tarequzzaman, R. Ferreira, S. Sievers, M. Bieler, and H. W. Schumacher, Electrical measurement of absolute temperature and temperature transients in a buried nanostructure under ultrafast optical heating, *Appl. Phys. Lett.* **110**, 232403 (2017).
- [7] N. Locatelli, V. Cros, and J. Grollier, Spin-torque building blocks, *Nat. Mater.* **13**, 11 (2014).
- [8] B. Fang, M. Carpentieri, X. Hao, H. Jiang, J. A. Katine, I. N. Krivorotov, B. Ocker, J. Langer, K. L. Wang, B. Zhang, B. Azzerboni, P. K. Amiri, G. Finocchio, and Z. Zeng, Giant spin-torque diode sensitivity in the absence of bias magnetic field, *Nat. Commun.* **7**, 11259 (2016).
- [9] M. Goto, Y. Wakatake, U. K. Oji, S. Miwa, N. Strelkov, B. Dieny, H. Kubota, K. Yakushiji, A. Fukushima, and S. Yuasa, Microwave amplification in a magnetic tunnel junction induced by heat-to-spin conversion at the nanoscale, *Nat. Nanotechnol.* **14**, 3 (2019).
- [10] M. Tarequzzaman, A. S. Jenkins, T. Böhnert, J. Borme, L. Martins, E. Paz, R. Ferreira, and P. P. Freitas, Broad-band voltage rectifier induced by linear bias dependence in CoFeB/MgO magnetic tunnel junctions, *Appl. Phys. Lett.* **112**, 252401 (2018).
- [11] W. A. Borders, A. Z. Pervaiz, S. Fukami, K. Y. Cam-sari, H. Ohno, and S. Datta, Integer factorization using stochastic magnetic tunnel junctions, *Nature* **573**, 390 (2019).
- [12] J. Torrejon, M. Riou, F. A. Araujo, S. Tsunegi, G. Khalsa, D. Querlioz, P. Bortolotti, V. Cros, K. Yakushiji, A. Fukushima, H. Kubota, S. Yuasa, M. D. Stiles, and J. Grollier, Neuromorphic computing with nanoscale spintronic oscillators, *Nature* **547**, 428 (2017).
- [13] B. Dieny and M. Chshiev, Perpendicular magnetic anisotropy at transition metal/oxide interfaces and applications, *Rev. Mod. Phys.* **89**, 025008 (2017).
- [14] S. Ikeda, K. Miura, H. Yamamoto, K. Mizunuma, H. D. Gan, M. Endo, S. Kanai, J. Hayakawa, F. Matsukura, and H. Ohno, A perpendicular-anisotropy CoFeB–MgO magnetic tunnel junction, *Nat. Mater.* **9**, 721 (2010).

- [15] S. Kanai, M. Tsujikawa, Y. Miura, M. Shirai, F. Matsukura, and H. Ohno, Magnetic anisotropy in Ta/CoFeB/MgO investigated by x-ray magnetic circular dichroism and first-principles calculation, *Appl. Phys. Lett.* **105**, 222409 (2015).
- [16] T. Ueno, J. Sinha, N. Inami, Y. Takeichi, and S. Mitani, Enhanced orbital magnetic moments in magnetic heterostructures with interface perpendicular magnetic anisotropy, *Sci. Rep.* **5**, 14858 (2015).
- [17] H. X. Yang, M. Chshiev, B. Dieny, J. H. Lee, A. Manchon, and K. H. Shin, First-principles investigation of the very large perpendicular magnetic anisotropy at Fe/MgO and Co/MgO interfaces, *Phys. Rev. B* **84**, 054401 (2011).
- [18] W. C. Tsai, S. C. Liao, H. C. Hou, C. T. Yen, Y. H. Wang, H. M. Tsai, F. H. Chang, H. J. Lin, and C.-H. Lai, Investigation of perpendicular magnetic anisotropy of CoFeB by x-ray magnetic circular dichroism, *Appl. Phys. Lett.* **100**, 172414 (2012).
- [19] L. Plucinski, Y. Zhao, B. Sinkovic, and E. Vescovo, MgO/Fe(100) interface: A study of the electronic structure, *Phys. Rev. B* **75**, 214411 (2007).
- [20] A.T. Hindmarch, K.J. Dempsey, D. Ciudad, E. Negusse, D.A. Arena, and C.H. Marrows, Fe diffusion, oxidation, and reduction at the CoFeB/MgO interface studied by soft x-ray absorption spectroscopy and magnetic circular dichroism, *Appl. Phys. Lett.* **96**, 092501 (2010).
- [21] D. Telesca, B. Sinkovic, S. H. Yang, and S. S. P. Parkin, X-ray studies of interface Fe-oxide in annealed MgO based magnetic tunneling junctions, *J. Electron Spectros. Relat. Phenomena* **185**, 133 (2012).
- [22] M. Li, S. Wang, S. Zhang, S. Fang, G. Feng, X. Cao, P. Zhang, B. Wang, and G. Yu, The effect of interfacial oxygen migration on the PMA and thermal stability in MTJ with double MgO layers, *Appl. Surf. Sci.* **488**, 30 (2019).
- [23] M. Bersweiler, E. C. I. Enobio, S. Fukami, H. Sato, and H. Ohno, An effect of capping-layer material on interfacial anisotropy and thermal stability factor of MgO/CoFeB/Ta/CoFeB/MgO/capping-layer structure, *Appl. Phys. Lett.* **113**, 172401 (2018).
- [24] H. Yang, S.-H. Yang, and S. Parkin, The role of Mg interface layer in MgO magnetic tunnel junctions with CoFe and CoFeB electrodes, *AIP Adv.* **2**, 012150 (2012).
- [25] S. Isogami, M. Tsunoda, K. Komagaki, K. Sunaga, Y. Uehara, M. Sato, T. Miyajima, and M. Takahashi, In situ heat treatment of ultrathin MgO layer for giant magnetoresistance ratio with low resistance area product in CoFeB/MgO/CoFeB magnetic tunnel junctions, *Appl. Phys. Lett.* **93**, 192109 (2008).
- [26] Y. Nagamine, H. Maehara, K. Tsunekawa, D. D. Djayaprawira, N. Watanabe, S. Yuasa, and K. Ando, Ultra-low resistance-area product of and high magnetoresistance above 50% in magnetic tunnel junctions, *Appl. Phys. Lett.* **89**, 162507 (2008).
- [27] J. Lourebam, B. Chen, A. Huang, S. Allauddin, and S. Ter Lim, A non-collinear double MgO based perpendicular magnetic tunnel junction, *Appl. Phys. Lett.* **113**, 022403 (2018).
- [28] M. Wang, W. Cai, K. Cao, J. Zhou, J. Wrona, S. Peng, H. Yang, J. Wei, W. Kang, Y. Zhang, J. Langer, B. Ocker, A. Fert, and W. Zhao, Current-induced magnetization switching in atom-thick tungsten engineered perpendicular magnetic tunnel junctions with large tunnel magnetoresistance, *Nat. Commun.* **9**, 671 (2018).
- [29] K. Watanabe, B. Jinnai, S. Fukami, H. Sato, and H. Ohno, Shape anisotropy revisited in single-digit nanometer magnetic tunnel junctions, *Nat. Commun.* **9**, 663 (2018).
- [30] S.-W. Chun, D. Kim, J. Kwon, B. Kim, H. Lee, and S.-B. Lee, Negative electron-beam resist hard mask ion beam etching process for the fabrication of nanoscale magnetic tunnel junctions, *J. Vac. Sci. Technol., B* **30**, 06FA01 (2012).
- [31] H. Honjo, M. Niwa, K. Nishioka, T. V. A. Nguyen, H. Naganuma, Y. Endo, M. Yasuhira, S. Ikeda, and T. Endoh, Influence of hard mask materials on the magnetic properties of perpendicular MTJs With double CoFeB/MgO interface, *IEEE Trans. Magn.* **56**, 6703504 (2020).
- [32] J. Lourebam, A. Ghosh, M. Zeng, S. K. Wong, Q. J. Yap, and S. T. Lim, Thickness-Dependent Perpendicular Magnetic Anisotropy and Gilbert Damping in Hf/Co₂₀Fe₆₀B₂₀/MgO Heterostructures, *Phys. Rev. Appl.* **10**, 044057 (2018).
- [33] M. T. Johnson, P. J. H. Blomen, F. J. A. den Broeder, and J. J. de Vries, Magnetic anisotropy in metallic multilayers, *Rep. Progr. Phys.* **59**, 1409 (1996).
- [34] R. C. O'Handley, *Modern Magnetic Materials: Principles and Applications* (Wiley, New York, 2000).
- [35] See the Supplemental Material at <http://link.aps.org/supplemental/10.1103/PhysRevApplied.14.054022> for hysteresis loops, correction of saturation effects, thickness-dependent K_{eff} , Co and O spectra, Co moments, spectra for sample ⑥, γ -Fe₂O₃ calculations, and background subtraction.
- [36] X. Yu, O. Wilhelmli, H. O. Moser, S. V. Vidharaj, X. Gao, A. T. S. Wee, T. Nyunt, H. Qian, and H. Zheng, New soft X-ray facility SINS for surface and nanoscale science at SSLS, *J. Electron Spectros. Relat. Phenomena* **144–147**, 1031 (2005).
- [37] M. Abbate, J. B. Goedkoop, F. M. F. de Groot, M. Grioni, C. Fuggle, S. Hofmann, H. Petersen, and M. Sacchi, Probing depth of soft X-ray absorption spectroscopy measured in total-electron-yield mode, *Surf. Interface Anal.* **18**, 65 (1992).
- [38] Y. U. Idzerda, C. T. Chen, H. J. Lin, G. Meigs, G. H. Ho, and C. C. Kao, Soft X-ray magnetic circular dichroism and magnetic films, *Nucl. Inst. Methods Phys. Res. A* **347**, 134 (1994).
- [39] D. J. Huang, C. F. Chang, H. T. Jeng, G. Y. Guo, H. J. Lin, W. B. Wu, H. C. Ku, A. Fujimori, Y. Takahashi, and C. T. Chen, Spin and orbital magnetic moments of Fe₃O₄, *Phys. Rev. Lett.* **93**, 077204 (2004).
- [40] J. Y. Kim, T. Y. Koo, and J. H. Park, Orbital and bonding anisotropy in a half-filled GaFeO₃ magnetoelectric ferrimagnet, *Phys. Rev. Lett.* **96**, 047205 (2006).
- [41] B. Zhang, L. Wu, J. Zheng, P. Yang, X. Yu, J. Ding, S. M. Heald, R. A. Rosenberg, T. V. Venkatesan, J. Chen, C. J. Sun, Y. Zhu, and G. M. Chow, Control of magnetic anisotropy by orbital hybridization with charge transfer in (La_{0.67}Sr_{0.33}MnO₃)_n/(SrTiO₃)_n superlattice, *NPG Asia Mater.* **10**, 931 (2018).
- [42] R. Nakajima, J. Stöhr, and Y. U. Idzerda, Electron-yield saturation effects in L-edge x-ray magnetic circular dichroism spectra of Fe, Co, and Ni, *Phys. Rev. B* **59**, 6421 (1999).

- [43] F. Jiménez-Villacorta, C. Prieto, Y. Huttel, N. D. Telling, and G. Van Der Laan, X-ray magnetic circular dichroism study of the blocking process in nanostructured iron-iron oxide core-shell systems, *Phys. Rev. B* **84**, 172404 (2011).
- [44] D. H. Kim, H. J. Lee, G. Kim, Y. S. Koo, J. H. Jung, H. J. Shin, J. Y. Kim, and J.-S. Kang, Interface electronic structures of BaTiO₃ @ X nanoparticles (X = γ -Fe₂O₃, Fe₃O₄, α -Fe₂O₃, and Fe) investigated by XAS and XMCD, *Phys. Rev. B* **79**, 033402 (2009).
- [45] T. S. Herng, W. Xiao, S. M. Poh, F. He, R. Sutarto, X. Zhu, and R. Li, Achieving a high magnetization in sub-nanostructured magnetite films by spin-flipping of tetrahedral Fe³⁺, *Nano Res.* **8**, 2935 (2015).
- [46] B. T. Thole, P. Carra, and F. Sette, And G. van der laan, X-ray circular dichroism as a probe of orbital magnetization, *Phys. Rev. Lett.* **68**, 1943 (1992).
- [47] C. T. Chen, Y. U. Idzerda, H.-J. Lin, N. V. Smith, G. Meigs, E. Chaban, G. H. Ho, E. Pellegrin, and F. Sette, Experimental confirmation of the X-Ray magnetic circular dichroism Sum rules for iron and cobalt, *Phys. Rev. Lett.* **75**, 152 (1995).
- [48] P. Torelli, S. Benedetti, P. Luches, L. Gragnaniello, J. Fujii, and S. Valeri, Morphology-induced magnetic phase transitions in Fe deposits on MgO films investigated with XMCD and STM, *Phys. Rev. B* **79**, 035408 (2009).
- [49] W. Kuch, J. Gilles, S. S. Kang, F. Offi, J. Kirschner, S. Imada, and S. Suga, Quantitative x-ray magnetic circular dichroism microspectroscopy of Fe/Co/Cu(001) using a photoemission microscope, *J. Appl. Phys.* **87**, 5747 (2000).
- [50] S. Baumann, F. Donati, S. Stepanow, S. Rusponi, W. Paul, S. Gangopadhyay, I. G. Rau, G. E. Pacchioni, L. Gragnaniello, M. Pivetta, J. Dreiser, C. Piamonteze, C. P. Lutz, R. M. Macfarlane, B. A. Jones, P. Gambardella, A. J. Heinrich, and H. Brune, Origin of perpendicular magnetic anisotropy and large orbital moment in Fe atoms on MgO, *Phys. Rev. Lett.* **115**, 237202 (2015).
- [51] F. M. F. de Groot, M. Grioni, J. C. Fuggle, J. Ghijsen, G. A. Sawatzky, and H. Petersen, Oxygen 1s x-ray-absorption edges of transition-metal oxides, *Phys. Rev. B* **40**, 5715 (1989).
- [52] M. Abbate, F. M. F. de Groot, J. C. Fuggle, A. Fujimori, O. Strebel, F. Lopez, M. Domke, G. Kaindl, G. A. Sawatzky, M. Takano, Y. Takeda, H. Eisaki, and S. Uchida, Controlled-valence properties of $La_{1-x}Sr_xFeO_3$ and $La_{1-x}Sr_xMnO_3$ studied by soft-x-ray absorption spectroscopy, *Phys. Rev. B* **46**, 4511 (1992).
- [53] P. Bruno, Tight-binding approach to the orbital magnetic moment and magnetocrystalline anisotropy of transition-metal monolayers, *Phys. Rev. B* **39**, 865 (1989).
- [54] J. Stöhr and H. C. Siegmann, *Magnetism: From Fundamentals to Nanoscale Dynamics* (Springer-Verlag, Berlin, 2006).
- [55] A. Grimaud, K. J. May, C. E. Carlton, Y. Lee, M. Risch, W. T. Hong, J. Zhou, and Y. Shao-horn, Double perovskites as a family of highly active catalysts for oxygen evolution in alkaline solution, *Nat. Commun.* **4**, 2439 (2013).
- [56] Y. Li, *et al.*, Electronic-reconstruction-enhanced hydrogen evolution catalysis in oxide polymorphs, *Nat. Commun.* **10**, 3149 (2019).
- [57] P. Luches, S. D'Addato, S. Valeri, E. Groppo, C. Prestipino, C. Lamberti, and F. Boscherini, X-ray absorption study at the Mg and O K edges of ultrathin MgO epilayers on Ag(001), *Phys. Rev. B* **69**, 045412 (2004).
- [58] S. Gautam, K. Asokan, J. P. Singh, F.-H. Chang, H.-J. Lin, and K. H. Chae, Electronic structure of Fe/MgO/Fe multilayer stack by X-ray magnetic circular dichroism, *J. Appl. Phys.* **115**, 17C109 (2014).
- [59] M. Zeng, J. Lourembam, and S. Ter Lim, Large electric field modulation of magnetic anisotropy in MgO/CoFe/Ta structures with monolayer oxide insertion, *Appl. Phys. Lett.* **113**, 192404 (2018).
- [60] C. T. Chen, F. Sette, Y. Ma, M. S. Hybertsen, E. B. Stechel, W. M. C. Foulkes, M. Schuller, S. W. Cheong, A. S. Cooper, L. W. Rupp, B. Batlogg, Y. L. Soo, Z. H. Ming, A. Krol, and Y. H. Kao, Electronic States in $La_{2-x}Sr_xCuO_{4+\delta}$ Probed By Soft-X-ray Absorption, *Phys. Rev. Lett.* **66**, 104 (1991).